

Model independent determination of the CKM phase γ using input from D^0 - \bar{D}^0 mixing

Samuel Harnew and Jonas Rademacker

H H Wills Physics Laboratory, University of Bristol, UK

E-mail: Sam.Harnew@bristol.ac.uk, Jonas.Rademacker@bristol.ac.uk

ABSTRACT: We present a new, amplitude model-independent method to measure the CP violation parameter γ in $B^- \rightarrow DK^-$ and related decays. Information on charm interference parameters, usually obtained from charm threshold data, is obtained from charm mixing. By splitting the phase space of the D meson decay into several bins, enough information can be gained to measure γ without input from the charm threshold. We demonstrate the feasibility of this approach with a simulation study of $B^- \rightarrow DK^-$ with $D \rightarrow K^+\pi^-\pi^+\pi^-$. We compare the performance of our novel approach to that of a previously proposed binned analysis which uses charm interference parameters obtained from threshold data. While both methods provide useful constraints, the combination of the two by far outperforms either of them applied on their own. Such an analysis would provide a highly competitive measurement of γ . Our simulation studies indicate, subject to assumptions about data yields and the amplitude structure of $D^0 \rightarrow K^+\pi^-\pi^+\pi^-$, a statistical uncertainty on γ of $\sim 12^\circ$ with existing data and $\sim 4^\circ$ for the LHCb-upgrade.

Contents

1	Introduction	2
2	Formalism	3
2.1	Phase-space integrated amplitudes and interference parameter	3
2.2	D mixing, time-dependent decay rates	4
2.3	$B^\mp \rightarrow DK^\mp$, γ , and \mathcal{Z}^f	5
2.4	Parameter counting using ratios	6
2.5	Parameter counting using rates	6
2.6	Multiple solutions	7
3	Amplitude models and binning	8
3.1	Amplitude model	8
3.2	Model-informed binning	8
4	Simulation studies	10
4.1	Simulated data samples	10
4.2	Fit method and parametrisation	11
4.3	Algorithms	12
4.4	Confidence regions in γ , δ_B , r_B and x_\pm , y_\pm	12
4.4.1	Using the wrong model	14
4.5	Studies with other models	15
4.6	Additional input from the charm threshold	16
4.6.1	Phase-space integrated analysis with input from the charm threshold	16
4.6.2	Global constraints from the charm threshold, with a binned $B^\mp \rightarrow DK^\mp$ and D mixing analysis	17
4.6.3	Binned constraints from the charm threshold	18
4.7	1-D scans and quantified uncertainties	19
4.8	Summary of results	20
5	Conclusion	21

1 Introduction

The measurement of γ from $B^- \rightarrow DK^-$, $D \rightarrow f$ [1–6] (where f represents a multibody final state accessible to both D^0 and \bar{D}^0) depends on the correct description of the interference between the $D^0 \rightarrow f$ and $\bar{D}^0 \rightarrow f$ decay amplitudes.¹ This can be obtained from an amplitude model of the D decay. However, this model dependence can lead to significant systematic uncertainties. Alternative model-independent methods use experimental input [7, 8] to remove this source of systematic uncertainty. This input can be summarised in the complex interference parameter $\mathcal{Z}^f = R_D^f e^{-i\delta_D^f}$, where R_D^f and δ_D^f are the coherence factor and average strong phase-difference introduced in [7]. \mathcal{Z}^f can be measured exploiting quantum-correlated $D\bar{D}$ pairs available at experiments operating at the charm threshold, like CLEO-c or BES III [7–14].

We found previously that input from charm mixing, when combined with constraints from threshold data, can substantially reduce the uncertainty on \mathcal{Z}^f [15]. In this letter we present a new method for an amplitude model-independent measurement of γ based on charm input from mixing that, by dividing the D decay’s phase space into multiple bins, extracts sufficient information to perform a model independent measurement of γ without input from charm threshold results. We verify the feasibility of this method using simulated data. We also study the performance of a binned analysis with charm input from the charm threshold, rather than mixing, as proposed in [7]. While both methods provide interesting constraints on γ and related parameters, we find that a combined approach far outperforms each method individually. Applied to $B^- \rightarrow DK^-$, $D \rightarrow K^- \pi^+ \pi^- \pi^+$, a substantially better precision on γ and related parameters can be achieved than with previously considered methods for this decay mode, potentially making this one of the most precise individual measurements.

This letter is organised as follows: based on the formalism described in [15] we show in Sec. 2 that, when the D decay’s phase space is divided into multiple bins, it is possible to extract γ from a simultaneous analysis of $B^\mp \rightarrow DK^\mp$ and D -mixing without input from charm threshold data. In Sec. 3.2 we discuss how to divide the five-dimensional phase space of $D \rightarrow K^- \pi^+ \pi^- \pi^+$ into bins in a way that optimises the sensitivity to γ . In Sec. 4 we present the results of a simulation study for the decay mode $B^- \rightarrow DK^-$, $D \rightarrow K^- \pi^+ \pi^- \pi^+$, using sample sizes corresponding to our estimates of plausible current and future LHCb event yields. We estimate the precision on γ and related parameters for various data taking scenarios and approaches, with and without input from the charm threshold. The key results of the simulation study are summarised in Sec. 4.8 (Tab. 2). In Sec. 5, we conclude.

¹Charged conjugate modes are implied throughout unless stated otherwise. The symbol D is used to represent any superposition of D^0 and \bar{D}^0 .

2 Formalism

2.1 Phase-space integrated amplitudes and interference parameter

The measurement of γ from $B^- \rightarrow DK^-$ [1–8] and the method for extracting \mathcal{Z}^f from mixing introduced in [15] both exploit the interference of D^0 and \bar{D}^0 decay amplitudes to the same final state $f_{\mathbf{p}}$, $\langle f_{\mathbf{p}} | \hat{H} | D^0 \rangle$ and $\langle f_{\mathbf{p}} | \hat{H} | \bar{D}^0 \rangle$. The subscript $\mathbf{p} = (p_1, \dots, p_n)$ identifies a point in n dimensional phase space, with $n = 3N_f - 7$ for a final state f with a particle content of N_f pseudoscalars. \hat{H} is the interaction Hamiltonian relevant for the decay. It is useful to define the magnitude of the ratio of these amplitudes, $r_{\mathbf{p}}$, and their phase difference $\delta_{\mathbf{p}}$, at phase-space point \mathbf{p} , through

$$r_{\mathbf{p}} e^{i\delta_{\mathbf{p}}} = \frac{\langle f_{\mathbf{p}} | \hat{H} | D^0 \rangle}{\langle f_{\mathbf{p}} | \hat{H} | \bar{D}^0 \rangle}. \quad (2.1)$$

The decay rates integrated over regions or bins of phase space, which we label with Ω , can be expressed in terms of the real, positive quantities

$$\mathcal{A}_{\Omega} \equiv \sqrt{\int_{\Omega} |\langle f_{\mathbf{p}} | \hat{H} | D^0 \rangle|^2 \left| \frac{\partial^n \phi}{\partial(p_1 \dots p_n)} \right| d^n p}, \quad \mathcal{B}_{\Omega} \equiv \sqrt{\int_{\Omega} |\langle f_{\mathbf{p}} | \hat{H} | \bar{D}^0 \rangle|^2 \left| \frac{\partial^n \phi}{\partial(p_1 \dots p_n)} \right| d^n p}, \quad (2.2)$$

and the complex parameter

$$\mathcal{Z}_{\Omega}^f \equiv \frac{1}{\mathcal{A}_{\Omega} \mathcal{B}_{\Omega}} \int_{\Omega} \langle f_{\mathbf{p}} | \hat{H} | D^0 \rangle \langle f_{\mathbf{p}} | \hat{H} | \bar{D}^0 \rangle^* \left| \frac{\partial^n \phi}{\partial(p_1 \dots p_n)} \right| d^n p. \quad (2.3)$$

In these expressions, $\left| \frac{\partial^n \phi}{\partial(p_1 \dots p_n)} \right|$ represents the density of states at phase space point \mathbf{p} . The complex interference parameter \mathcal{Z}_{Ω}^f has a magnitude between 0 and 1. It encodes the relevant interference effects in phase-space region Ω . As the integrand in the definition of \mathcal{Z}_{Ω}^f is proportional to $e^{i\delta_{\mathbf{p}}}$, $|\mathcal{Z}_{\Omega}^f|$ is maximal if $\delta_{\mathbf{p}}$ is constant over the integration region, while highly fluctuating $\delta_{\mathbf{p}}$ tends to result in small $|\mathcal{Z}_{\Omega}^f|$. The complex interference parameter \mathcal{Z}_{Ω}^f can also be expressed in terms of the coherence factor R_{Ω}^f and average strong phase difference δ_{Ω}^f introduced in [7], or in terms of the c_{Ω} and s_{Ω} parameters introduced in [8]:

$$\mathcal{Z}_{\Omega}^f = R_{\Omega}^f e^{-i\delta_{\Omega}^f} = c_{\Omega} + i s_{\Omega}. \quad (2.4)$$

Equation 2.4 implies a normalisation of c_{Ω} and s_{Ω} that differs from that in the original paper [8], but corresponds to the one used in most subsequent publications [10, 11, 16–18].

2.2 D mixing, time-dependent decay rates

For simplicity, we assume CP conservation in the neutral D system, which has been shown to be a valid assumption to a frustrating degree of accuracy [19, 20]. The general case is described for example in [15]. We use the following convention for the definition of the CP even and odd D eigenstates, D_+ and D_- :

$$|D_{\pm}\rangle = |D^0\rangle \pm |\bar{D}^0\rangle \quad (2.5)$$

which have masses M_{\pm} and widths Γ_{\pm} . We also define the mean lifetime Γ_D and the usual dimensionless mixing parameters x and y :

$$\Gamma_D \equiv \frac{1}{2}(\Gamma_- + \Gamma_+), \quad x \equiv \frac{M_- - M_+}{\Gamma}, \quad y \equiv \frac{\Gamma_- - \Gamma_+}{2\Gamma}. \quad (2.6)$$

The mixing parameters x and y are both small, approximately half a percent [19–26]. The above definitions imply CP $|D^0\rangle = +|\bar{D}^0\rangle$. An alternative choice would be CP $|D^0\rangle = -|\bar{D}^0\rangle$, resulting in a phase-shift of \mathcal{Z}_{Ω}^f , defined in Eq. 2.3, by π [15].

Although the method presented here is in principle applicable to any D decay to a final state accessible to both D^0 and \bar{D}^0 , we will restrict ourselves from here on to the case where $\langle f_{\mathbf{p}}|\hat{H}|D^0\rangle$ is doubly Cabibbo suppressed (DCS) and $\langle f_{\mathbf{p}}|\hat{H}|\bar{D}^0\rangle$ is Cabibbo favoured (CF), as is the case for $f = K^+\pi^-\pi^+\pi^-$. Such decays have the advantage that for the suppressed, “wrong sign” (WS) decay, the mixing-induced amplitude $A(D^0 \rightarrow \bar{D}^0 \rightarrow f)$ and the direct amplitude $A(D^0 \rightarrow f)$ are of comparable magnitude, leading to large interference effects, and high sensitivity to \mathcal{Z}^f . On the other hand, the “right sign” (RS) decay $D^0 \rightarrow \bar{f}$ is completely dominated by the CF amplitude, with negligible interference effects, and thus provides an excellent normalisation mode. For this case

$$r_{D,\Omega} \equiv \frac{\mathcal{A}_{\Omega}^{DCS}}{\mathcal{B}_{\Omega}^{CF}} \ll 1. \quad (2.7)$$

where \mathcal{A}_{Ω} , \mathcal{B}_{Ω} are defined in Eq. 2.2; the superscripts are added for clarity. The time dependent rates for a D meson that was a D^0 or a \bar{D}^0 at time $t_0 = 0$, to decay to a final state f within the phase-space volume Ω at proper time t are given, up to third order in the small parameters x , y and $r_{D,\Omega}$, by

$$\Gamma(D^0(t) \rightarrow f)_{\Omega} \simeq \left[\mathcal{A}_{\Omega}^2 + \mathcal{A}_{\Omega}\mathcal{B}_{\Omega} \left(y \text{Re} \mathcal{Z}_{\Omega}^f + x \text{Im} \mathcal{Z}_{\Omega}^f \right) \Gamma_D t + \mathcal{B}_{\Omega}^2 \frac{x^2 + y^2}{4} (\Gamma_D t)^2 \right] e^{-\Gamma_D t}, \quad (2.8)$$

for the WS rate, and

$$\Gamma(\bar{D}^0(t) \rightarrow f)_{\Omega} \simeq \mathcal{B}_{\Omega}^2 e^{-\Gamma_D t} \quad (2.9)$$

for the RS rate, with corresponding expressions for the CP conjugate modes. Many detector effects cancel in the ratio of WS to RS decays, given by

$$\frac{\Gamma(D^0(t) \rightarrow f)_\Omega}{\Gamma(\bar{D}^0(t) \rightarrow f)_\Omega} = r_{D,\Omega}^2 + r_{D,\Omega} \left(y \text{Re} \mathcal{Z}_\Omega^f + x \text{Im} \mathcal{Z}_\Omega^f \right) (\Gamma_{Dt}) + \frac{x^2 + y^2}{4} (\Gamma_{Dt})^2. \quad (2.10)$$

2.3 $B^\mp \rightarrow DK^\mp$, γ , and \mathcal{Z}^f

The decay $B^- \rightarrow DK^-$, and related decays, provide a particularly clean way of measuring the CKM phase γ . The details of the analysis depend considerably on the final state f of the subsequent D decay, which must be accessible to both D^0 and \bar{D}^0 [1–6]. The sensitivity to γ arises from the interference of the decay amplitudes with the intermediary states $D^0 K^-$ and $\bar{D}^0 K^-$, which we express as:

$$\begin{aligned} \mathcal{F}_+ &\equiv \langle \bar{D}^0 K^+ | \hat{H} | B^+ \rangle, & \mathcal{S}_+ &\equiv \langle D^0 K^+ | \hat{H} | B^+ \rangle, \\ \mathcal{F}_- &\equiv \langle D^0 K^- | \hat{H} | B^- \rangle, & \mathcal{S}_- &\equiv \langle \bar{D}^0 K^- | \hat{H} | B^- \rangle. \end{aligned} \quad (2.11)$$

where \mathcal{F} denotes colour and CKM favoured amplitudes, while \mathcal{S} denotes colour and CKM suppressed amplitudes. The ratios of the suppressed to favoured amplitudes are given by

$$r_B e^{i(\delta_B - \gamma)} = \frac{\mathcal{S}_-}{\mathcal{F}_-} \qquad r_B e^{i(\delta_B + \gamma)} = \frac{\mathcal{S}_+}{\mathcal{F}_+} \quad (2.12)$$

where r_B is the magnitude of those ratios, while δ_B and $\mp\gamma$ are their strong and weak phase differences respectively.

Because r_B is small (~ 0.1 [27, 28]), the interference effects and thus the sensitivity to γ in $B^- \rightarrow DK^-, D \rightarrow f$, are enhanced if a final state is chosen such that $D^0 \rightarrow f$ is doubly Cabibbo suppressed, while $\bar{D}^0 \rightarrow f$ is Cabibbo favoured [3], at the cost of an overall low decay rate. The time and phase space integrated decay rate for these suppressed B^\mp decays is given by

$$\Gamma(B^- \rightarrow DK^-, D \rightarrow f)_\Omega \simeq \mathcal{F}^2 \mathcal{A}_\Omega^2 + \mathcal{S}^2 \mathcal{B}_\Omega^2 + \mathcal{F} \mathcal{S} \mathcal{A}_\Omega \mathcal{B}_\Omega \left| \mathcal{Z}_\Omega^f \right| \cos(\delta_B - \delta_\Omega^f - \gamma) \quad (2.13)$$

$$\Gamma(B^+ \rightarrow DK^+, D \rightarrow \bar{f})_{\bar{\Omega}} \simeq \mathcal{F}^2 \mathcal{A}_{\bar{\Omega}}^2 + \mathcal{S}^2 \mathcal{B}_{\bar{\Omega}}^2 + \mathcal{F} \mathcal{S} \mathcal{A}_{\bar{\Omega}} \mathcal{B}_{\bar{\Omega}} \left| \mathcal{Z}_{\bar{\Omega}}^f \right| \cos(\delta_B - \delta_{\bar{\Omega}}^f + \gamma) \quad (2.14)$$

The corresponding favoured decay $B^- \rightarrow DK^-, D \rightarrow \bar{f}$ is completely dominated by the favoured decay amplitude with negligible interference effects and negligible sensitivity to γ , and has a much larger branching fraction. It therefore provides an ideal normalisation or control mode. Its time and phase-space integrated rate is given by:

$$\Gamma(B^- \rightarrow DK^-, D \rightarrow \bar{f})_{\bar{\Omega}} \simeq \Gamma(B^+ \rightarrow DK^+, D \rightarrow f)_\Omega \simeq \mathcal{F}^2 \mathcal{B}_\Omega^2 \quad (2.15)$$

The ratios of the favoured and suppressed rates are given by

$$\frac{\Gamma(B^- \rightarrow DK^-, D \rightarrow f)_\Omega}{\Gamma(B^- \rightarrow DK^-, D \rightarrow \bar{f})_{\bar{\Omega}}} = r_{D,\Omega}^2 + r_B^2 + r_{D,\Omega}r_B \left| \mathcal{Z}_\Omega^f \right| \cos(\delta_B - \delta_\Omega^f - \gamma) \quad (2.16)$$

$$\frac{\Gamma(B^+ \rightarrow DK^+, D \rightarrow \bar{f})_{\bar{\Omega}}}{\Gamma(B^+ \rightarrow DK^+, D \rightarrow f)_\Omega} = r_{D,\Omega}^2 + r_B^2 + r_{D,\Omega}r_B \left| \mathcal{Z}_\Omega^f \right| \cos(\delta_B - \delta_\Omega^f + \gamma). \quad (2.17)$$

These can also be expressed in terms of the Cartesian coordinates

$$x_\pm \equiv \text{Re} \left(r_B e^{i(\delta_B \pm \gamma)} \right) \quad y_\pm \equiv \text{Im} \left(r_B e^{i(\delta_B \pm \gamma)} \right) \quad (2.18)$$

using the relations

$$r_B \left| \mathcal{Z}_\Omega^f \right| \cos(\delta_B - \delta_\Omega^f \pm \gamma) = x_\pm \text{Re} \mathcal{Z}_\Omega^f + y_\pm \text{Im} \mathcal{Z}_\Omega^f \quad \text{and} \quad r_B^2 = x_\pm^2 + y_\pm^2. \quad (2.19)$$

Effects due to D^0 - \bar{D}^0 mixing have been ignored in the expressions for the $B^\mp \rightarrow DK^\mp$, $D \rightarrow f(\bar{f})$ decay rates, which is justified given the expected statistical precision. These effects can be included if required [29].

2.4 Parameter counting using ratios

Taking Γ_D , x , and y from external inputs, Eqs. 2.10, 2.16, 2.17 depend on three unknown parameters for each pair of CP -conjugate phase space bins $(\Omega, \bar{\Omega})$: $r_{D,\Omega}$, $\text{Re} \mathcal{Z}_\Omega^f$ and $\text{Im} \mathcal{Z}_\Omega^f$; and three that are the same in all bins: γ , δ_B and r_B . The time-dependent fit to the tagged charm decay rates (Eq. 2.10) provides two constraints on these parameters for each bin (the constant and the coefficient of the linear term). The $B^\mp \rightarrow DK^\mp$ decay rate ratios (Eqs. 2.16, 2.17) provide another two constraints. For N bin pairs, there are therefore $4N$ constraints and $3N + 3$ unknown parameters. To extract all unknown parameters from the data therefore requires $4N \geq 3N + 3 \Leftrightarrow N \geq 3$. If instead we wish to measure x_\pm, y_\pm , we need $N \geq 4$.

2.5 Parameter counting using rates

Taking again Γ_D , x , and y from external inputs, Eqs. 2.8, 2.9, 2.13, 2.14, 2.15 depend on four unknown parameters for each pair of CP -conjugate phase space bins: \mathcal{A}_Ω^2 , \mathcal{B}_Ω^2 , $\text{Re} \mathcal{Z}_\Omega^f$, and $\text{Im} \mathcal{Z}_\Omega^f$; and four that are the same in all bins: γ , δ_B , $r_B = \mathcal{S}/\mathcal{F}$, \mathcal{F}^2 . Eqs. 2.8 - 2.9 provide three constraints for each bin, and Eqs. 2.13 - 2.15 another three. Hence, to extract all of these parameters, we require $6N \geq 4N + 4 \Leftrightarrow N \geq 2$. A fit to extract x_\pm, y_\pm requires $N \geq 3$.

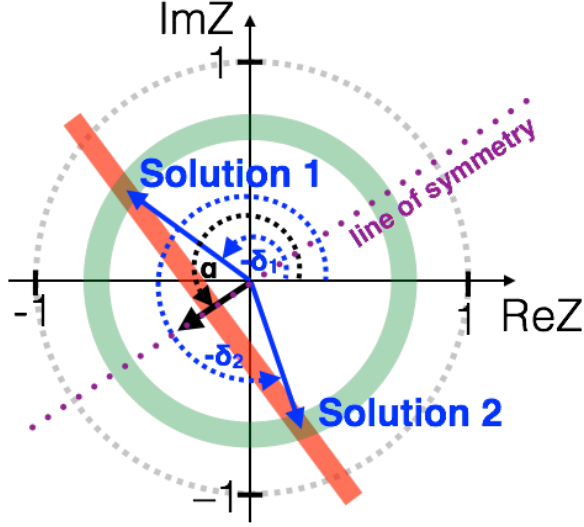


Figure 1. The combined constraints on $Z_\Omega^f = R_\Omega^f e^{-i\delta_\Omega^f}$ from charm mixing (red line with slope $-y/x$) and $B^\mp \rightarrow DK^\mp$ (green solid circle) lead to two possible solutions, whose sum (short black arrow) is always perpendicular to the charm constraint. (In the figure, the subscript Ω and superscript f are omitted for clarity.) The grey broken circular line indicates the boundary of the physically allowed region.

2.6 Multiple solutions

As described in [15], the charm mixing input constrains each $Z_\Omega^f = R_\Omega^f e^{-i\delta_\Omega^f}$ to a line of slope $-y/x$ in the $ReZ_\Omega^f - ImZ_\Omega^f$ plane. The input from the $B^\mp \rightarrow DK^\mp$ adds information on the magnitude of Z_Ω^f , leaving two possible solutions for each Z_Ω^f , which have the same magnitude but different phases: $-\delta_{\Omega 1}^f$ and $-\delta_{\Omega 2}^f$, as illustrated in Fig. 1. These solutions are symmetric with respect to a line of symmetry that is perpendicular to the constraint from charm mixing. Their sum is always along this line of symmetry and has the phase $\alpha = -\frac{1}{2}(\delta_{\Omega 1}^f + \delta_{\Omega 2}^f)$. Because α depends only on the charm mixing parameters (with $\tan \alpha = x/y$) it is the same for all phase-space bins. It is easy to show that, as a consequence of this relationship, the system of equations remains invariant under the following operation:

$$\left(\left\{ \delta_\Omega^f \right\}, \delta_B, \gamma \right) \rightarrow \left(\left\{ -2\alpha - \delta_\Omega^f \right\}, -2\alpha - \delta_B, -\gamma \right). \quad (2.20)$$

There is also the more obvious invariance under the simultaneous shift by π of δ_B and γ :

$$\left(\left\{ \delta_\Omega^f \right\}, \delta_B, \gamma \right) \rightarrow \left(\left\{ \delta_\Omega^f \right\}, \delta_B + \pi, \gamma + \pi \right), \quad (2.21)$$

leading to an overall four-fold ambiguity in γ and δ_B . In Sec. 4.6 we show how external input from the charm threshold [9, 14] can be used to reduce this to a 2-fold ambiguity.

3 Amplitude models and binning

3.1 Amplitude model

Up to this point, the discussion has not been specific to any particular final state of the D decay. For the remainder of this letter, we will require a specific amplitude model to test the binning method (Sec. 3.2) and perform simulation studies (Sec. 4). We will concentrate on the case where the D meson decays to $K^\pm\pi^\mp\pi^\pm\pi^\mp$. Our amplitude model for the CF $\bar{D}^0 \rightarrow K^+\pi^-\pi^+\pi^-$ decay is based on that found by the MARK III experiment [30]. There is currently no model available for the DCS decay $D^0 \rightarrow K^+\pi^-\pi^+\pi^-$. Any experiment in a position to use the method described here would have sufficient DCS decays to obtain such a model. For the purpose of this study, we have created a series of plausible DCS models by randomly varying the magnitudes and phases of the amplitude components of MARK III's CF model. Amongst these we select a representative sample of 100 DCS models that give, together with the MARK III model for the CF decay, global complex coherence parameters $\mathcal{Z}^{K3\pi}$ distributed approximately according to the CLEO-c measurement [14]. Most studies are based on our default model, which we chose based on its $\mathcal{Z}^{K3\pi}$ value of $0.26 + i0.24 = 0.36e^{i(42\pi/180)}$, which matches the central value measured in [14].

3.2 Model-informed binning

The model-independent method for measuring γ described in Sec. 2 relies on dividing the $D^0 \rightarrow f$ phase space, which is five dimensional for $D \rightarrow K^-\pi^+\pi^-\pi^+$, into several bins. In principle, any binning will work, for example the rectangular five dimensional binning used in [31]. However, to optimise the sensitivity of our approach, we follow the ideas for a model-informed binning described in [16, 32]. Because \mathcal{Z}_Ω^f is a factor in all γ sensitive terms, the sensitivity to γ increases with larger values of $|\mathcal{Z}_\Omega^f|$ in each bin. A strategy that ensures large $|\mathcal{Z}_\Omega^f|$ is to split phase space into bins of similar phase difference δ_p . We use an amplitude model to assign a value of δ_p to each event. The optimised binning is then achieved by splitting the one-dimensional δ_p distribution into continuous intervals, each of which constitutes one bin (which could in principle be discontinuous in 5-dimensional phase space). We choose the size of the intervals such that there is a similar number of suppressed $B^\mp \rightarrow DK^\mp$ events in each bin. A wrong model would result in a sub-optimal binning, resulting in smaller, but still model-independently measured, $|\mathcal{Z}_\Omega^f|$ in each bin. While this would reduce the sensitivity,

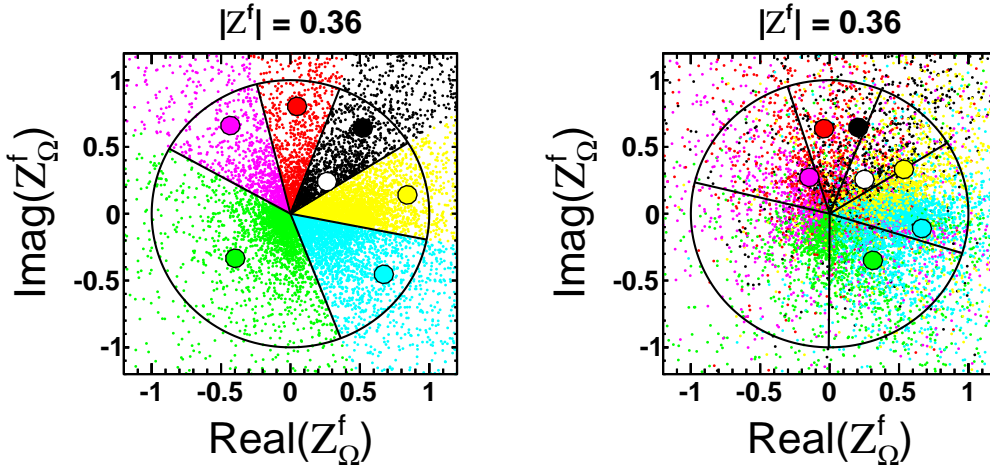


Figure 2. The plot shows simulated events (small dots), complex coherence parameters $Z_{\Omega}^{K3\pi}$ (colour-filled circles) for each bin, and the global coherence parameters $\mathcal{Z}^{K3\pi}$ (white-filled circle), represented in the $Re\mathcal{Z}^{K3\pi}-Im\mathcal{Z}^{K3\pi}$ plane, with bin assignments based on a perfect and an imperfect amplitude model, as described in the text.

which would be evident from the statistical uncertainty estimated from the fit, it would not introduce a model-dependent bias. Figure 2 shows the binned $Z_{\Omega}^{K3\pi}$ obtained from the default model, on the left hand side for a binning based on a perfect model and on the right for a binning based on an imperfect model. The perfect model is identical to the one used for the event generation. The imperfect model is obtained from the perfect one by multiplying each amplitude component’s magnitude by a random factor between 0.8 and 1.2 (corresponding to a fit fraction variation of 0.64 – 1.44), and by adding to each component a random phase between -0.3 and $+0.3$ radians. Figure 2 shows simulated events represented in the $Re\mathcal{Z}^{K3\pi}-Im\mathcal{Z}^{K3\pi}$ plane. The events are generated according to the phase space density of states. The position of the small dots represents the true value of $\frac{1}{\mathcal{A}_{\Omega}\mathcal{B}_{\Omega}}\langle f_{\mathbf{p}}|\hat{H}|D^0\rangle\langle f_{\mathbf{p}}|\hat{H}|\bar{D}^0\rangle^*$, while the colour-coding represents the bin they have been assigned to. For the left hand plot, this assignment is done with the perfect model, for the right hand plot with an imperfect model. The circular “pie chart” represents the bins in $\delta_{\mathbf{p}}$ based on the model used for the binning. The $Z_{\Omega}^{K3\pi}$ values extracted are the average over the true values of $\frac{1}{\mathcal{A}_{\Omega}\mathcal{B}_{\Omega}}\langle f_{\mathbf{p}}|\hat{H}|D^0\rangle\langle f_{\mathbf{p}}|\hat{H}|\bar{D}^0\rangle^*$ for the events in the bin they have been assigned to (which includes events beyond the plot boundaries). The model-independent method proposed above does of course not require the knowledge of $\frac{1}{\mathcal{A}_{\Omega}\mathcal{B}_{\Omega}}\langle f_{\mathbf{p}}|\hat{H}|D^0\rangle\langle f_{\mathbf{p}}|\hat{H}|\bar{D}^0\rangle^*$ to measure $Z_{\Omega}^{K3\pi}$, this information is only used for this illustration. The $Z_{\Omega}^{K3\pi}$ values are shown as colour-filled circles. The global complex coherence parameter $\mathcal{Z}^{K3\pi}$ is shown as a white-filled circle. While

the imperfect model leads to smaller $|Z_{\Omega}^{K3\pi}|$, they are still on average larger than the global $|\mathcal{Z}^{K3\pi}|$.

To quantify this observation, we repeated the study with the full set of 100 representative models and different numbers of bins. The results are summarised in Fig. 3

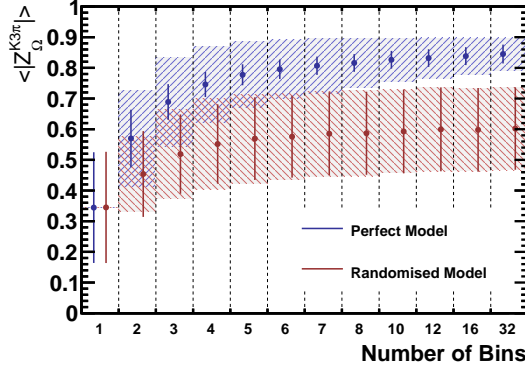


Figure 3. The average coherence factor with different number of bins in strong phase difference, for the set of 100 representative models, with perfect binning (blue, on top) and imperfect binning described in the text (red, lower). The error bars represent the standard deviation of the mean $Z_{\Omega}^{K3\pi}$ of each model, i.e. they represent the “between model scatter”. The shaded areas represent the average of the standard deviation of $Z_{\Omega}^{K3\pi}$ within the models (i.e. the “within model scatter”).

which shows the average $|Z_{\Omega}^{K3\pi}|$ as a function of the number of bins for the case where the binning is based on a perfect model, and for the case where the model used for binning is randomised as described above. The study shows that even a rather “bad” model provides typical binned coherence factors that are substantially larger than the global coherence factor.

4 Simulation studies

In order to demonstrate the validity of our method, and to evaluate its sensitivity, we perform fits to simulated data.

4.1 Simulated data samples

The data are generated according to the CF amplitude model based on the MARK III analysis of $D^0 \rightarrow K^- \pi^+ \pi^- \pi^+$ [30]. For the DCS amplitude describing $D^0 \rightarrow K^+ \pi^- \pi^+ \pi^-$ we choose from the large number of models we generated (see Sec. 3.2) the one that, when combined with the CF model, reproduces best the measured value of $\mathcal{Z}^{K3\pi}$ [14]

	$B^\pm \rightarrow D(K3\pi)K^\pm$		$D^{*\pm} \rightarrow$
	suppressed	favoured	$D(K3\pi)\pi^\pm$
LHCb run I (3 fb^{-1} @ $7 - 8\text{ TeV}$)	120	10k	8M
LHCb run II (8 fb^{-1} @ 13 TeV)	800	60k	50M
LHCb upgrade (50 fb^{-1} @ 13 TeV)	9000	700k	600M

Table 1. Event yields assumed in the simulation studies, based on reported event yields for 1 fb^{-1} at LHCb [31, 33]. The event yields are inclusive, for example, LHCb run II yields includes those from LHCb run I. The fraction of WS events in $D^{*\pm} \rightarrow D(K3\pi)\pi^\pm$ depends on the input variables; typically it is 0.38%.

as our default model. We also consider other DCS models to evaluate the stability of our results.

We study three scenarios with different event yields, based on plausible extrapolations of the yields reported for 1 fb^{-1} at LHCb [31, 33]: “LHCb run I”, where we extrapolate event yields to LHCb’s already recorded 3 fb^{-1} ; “LHCb run II”, plausible event yields at the end of the next LHC data taking period with approximately twice the collision energy; and “LHCb upgrade”, estimated event yields for the LHCb upgrade. We take into account the increase in the heavy flavour cross section at higher collision energies, and the expected improvement in trigger efficiency at the LHCb upgrade [34]. The sample sizes we use in our simulation studies, are given in Tab. 1. These extrapolations have of course large uncertainties.

We take into account the time-dependent detection efficiency that is typical for hadronic heavy flavour decays at LHCb, where the trigger is based on detecting displaced vertices, disfavouring small decay times. We use the same efficiency function as in [15]. We ignore all other detector effects and backgrounds, given the clean data samples at LHCb even for the suppressed $B^\pm \rightarrow D(K3\pi)K^\pm$ modes [33], this is a reasonable simplification for the purpose of these feasibility studies. Simulated data are generated with the following parameter values: $\gamma = 69.7^\circ$, $\delta_B = 112.0^\circ$, $r_B = 0.0919$, and $r_D^2 = \frac{1}{300}$.

4.2 Fit method and parametrisation

Our default approach is to perform a simultaneous χ^2 fit to the decay rates Eqs. 2.8, 2.9, 2.13, 2.13 and 2.15 in terms of the fit parameters $r_{D,\Omega}$, $Re\mathcal{Z}_\Omega^f$, $Im\mathcal{Z}_\Omega^f$, \mathcal{B}_Ω , \mathcal{F} , γ , δ_B and r_B . As a cross check, we also performed binned likelihood fits and found that they lead to equivalent results, but take longer to converge.

As long as all phase space bins are well populated, we find that the fit results are not crucially dependent on the number of bins. In our default scenario we divide phase

space into 4 bins for Run I, 6 bins for Run II and 8 bins for the upgrade.

We allow the charm mixing parameters x and y to vary in the fit, but constrain their value with a two-dimensional Gaussian constraint to their world-average using, for the LHCb Run I scenario [35]:

$$x = 0.526 \pm 0.161\% \quad y = 0.668 \pm 0.088\% \quad \rho_{xy} = 0.188, \quad (4.1)$$

where ρ_{xy} is the correlation coefficient between x and y . We expect substantial improvements on this measurement from LHCb, its upgrade, and BELLE-II in the future. Lacking detailed forecasts, for the purpose of this study, we assume that the uncertainties on x and y scale with the inverse square-root of LHCb event yields of the relevant data taking scenario, while the correlation coefficient remains constant. We fix the well-measured average D lifetime to $\tau_D = 1/\Gamma_D = 410.1$ fs [36].

While the default approach is to fit the decay rates, in an experimental measurement it may be favourable to fit the decay rate ratios Eqs. 2.10, 2.16 and 2.17. In this case we lose sensitivity to the parameters \mathcal{B}_Ω and \mathcal{F} . Using both fit methods on the same simulated dataset, we find that both approaches give the same results on the parameters they share. In Sec. 4.6 we will demonstrate how fitting the rates, as opposed to the ratios, allows us to add additional constraints to the fit.

4.3 Algorithms

In order to cope with the various local χ^2 minima that are present in addition to the four global minima, we use a two-stage fitting process. The first step is a fit with the GENEVA [37] package which is specifically designed to deal with multiple minima. We use GENEVA's parameter estimates as input to MINUIT [38] and perform a second fit to refine the parameter estimate. To further reduce the risk of converging on false minima, we repeat this process 75 times with many randomly chosen starting values for all fit parameters. Finally, we choose the fit result that gives the smallest χ^2 as our central value. In order to avoid unphysical values of \mathcal{Z}_Ω^f , which also can lead to further secondary minima, we add for each volume Ω a term that increases the χ^2 if \mathcal{Z}_Ω^f leaves the physical region:

$$\chi_{\text{constr } \mathcal{Z}_\Omega^f}^2 = \left\{ \begin{array}{ll} \left((|\mathcal{Z}_\Omega^f| - 1)/0.5 \right)^2 & \text{if } |\mathcal{Z}_\Omega^f| > 1 \\ 0 & \text{else} \end{array} \right\} \quad (4.2)$$

4.4 Confidence regions in γ , δ_B , r_B and x_\pm , y_\pm

We construct confidence regions in the parameters of interest based on the χ^2 difference, $\Delta\chi^2$, of the fit where the relevant parameters are fixed to the values to be probed,

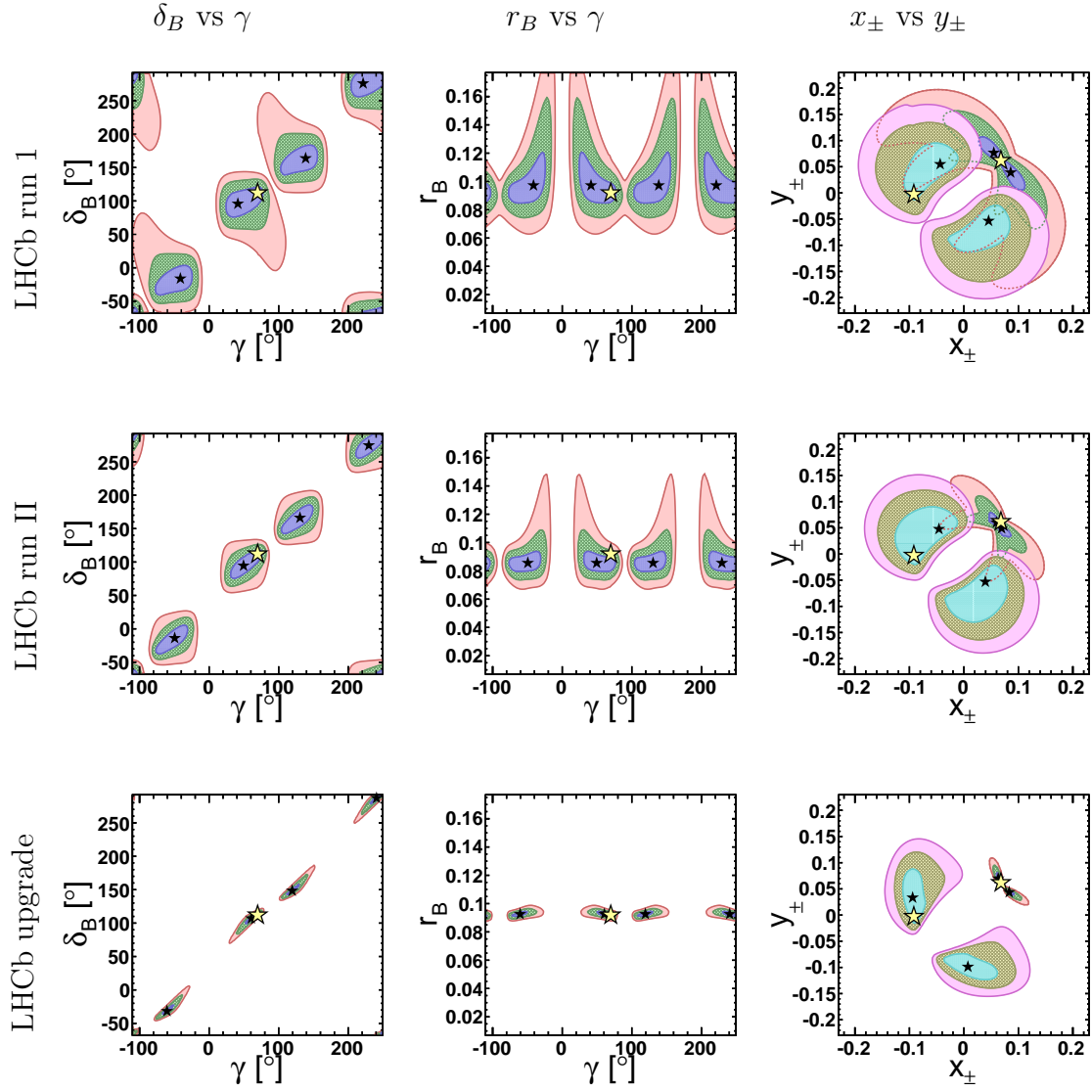


Figure 4. Confidence-level scans for γ , δ and r_B in the first two columns, and x_{\pm}, y_{\pm} in the third column, for simulated events according to the different scenarios given in Tab. 1. The 2 - D plots show $\sqrt{\Delta\chi^2} = 1, 2, 3$ contours. The yellow star indicates the input value and the black stars the (multiple) χ^2 minima. When secondary local minima are present, as in Figures 5 and 9, we indicate their positions with black crosses. The plots in the last column show contours for x_+, y_+ (with minima in the second and fourth quadrant) and x_-, y_- (with two minima in the first quadrant).

relative to the χ^2 of the best fit result when all parameters float. With $\sigma \equiv \sqrt{\Delta\chi^2}$, the probability or confidence level, CL, that the true value of the fit parameter is amongst

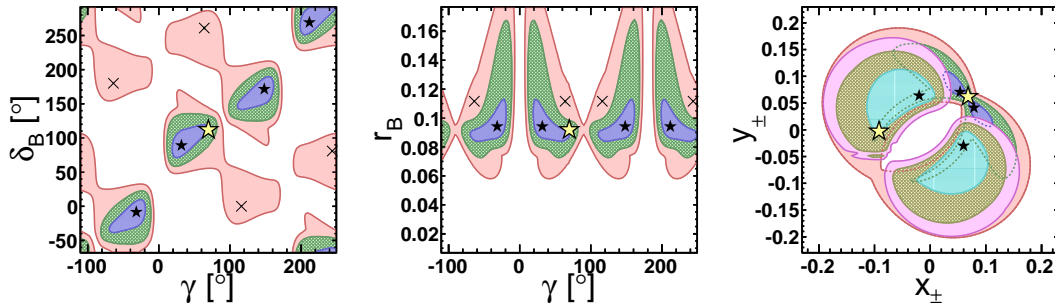


Figure 5. CL scans for simulated data generated with the default model, but binned based on the randomised model described in Sec. 3.2 (same format as in Fig. 4).

those with a smaller χ^2 is approximately

$$\text{CL} = 1 - p = \frac{1}{\sqrt{2\pi}} \int_{-\sigma}^{+\sigma} e^{-\frac{1}{2}y^2} dy \quad (4.3)$$

justifying the interpretation of σ in terms of Gaussian confidence levels. Equation 4.3 also defines the p -value, used in Sec. 4.7. We tested the applicability of Eq. 4.3 to our fit in extensive simulation studies. We observe good coverage for the default amplitude model and the vast majority of other amplitude models, for all three data taking scenarios. Amongst the large number of amplitude models we consider, there are however some where we find significant deviations from exact coverage (mostly over-coverage), suggesting that these studies ought to be repeated once an amplitude model has been obtained from data.

Figure 4 shows 2-dimensional scans in terms of 1, 2, 3 σ confidence regions for γ vs δ , γ vs r_B , and y_{\pm} vs x_{\pm} for each of the three data taking scenarios. The results show that the precision on x_{-} , y_{-} (or $\delta - \gamma$) is much better than that on x_{+} , y_{+} (or $\delta + \gamma$). We found this behaviour in many of the D amplitude models we studied (see Fig. 6), and that it appears to depend predominantly on the values for δ_B , and γ .

4.4.1 Using the wrong model

To study the impact of an imperfect binning, we repeated the sensitivity study using the imperfect binning discussed in Sec. 3.2, and applied it to our default Run II scenario. Comparing the results, shown in Fig. 5, to those in Fig. 4 shows that the imperfect binning results in a visible reduction in sensitivity especially at the 3 σ level, but it does not lead to a catastrophic deterioration of the fit, which retains a similar precision at the 1 σ level.

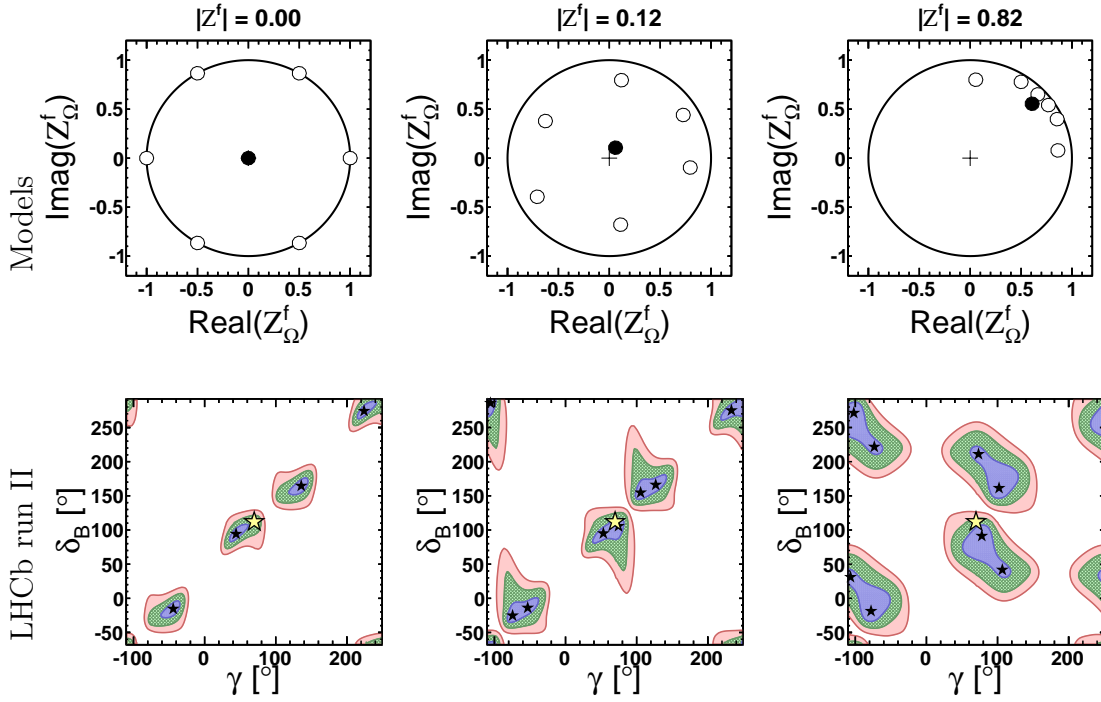


Figure 6. CL scans for three alternative models, for the LHCb run II data taking scenario. The top row shows the $Z_{\Omega}^{K3\pi}$ values and the central value of $\mathcal{Z}^{K3\pi}$ for the each model. The second row show the CL scans in the $\gamma - \delta_B$ plane, for the LHCb run II scenario.

4.5 Studies with other models

To study the dependence of our results on the particular amplitude model for the DCS $D^0 \rightarrow K^+\pi^-\pi^+\pi^-$ decay, we repeated the studies with a variety of amplitude models. CL scans in the $\gamma - \delta_B$ plane for three examples, for the LHCb run II data taking scenario, are shown in Fig. 6. The first column shows an artificial “ideal” model, set up to have bins with evenly distributed δ_{Ω}^f , and $|Z_{\Omega}^f| = 1$, $\mathcal{B}_{\Omega} = 1$, $\mathcal{A}_{\Omega} = r_{Df}$ for all Ω ; this also implies $|Z^f| = 0$. The second and third column show models taken from the set of randomly generated models; one where $|\mathcal{Z}^{K3\pi}|$ is smaller than CLEO-c’s central value, and another where it is larger. The results illustrate a general tendency we observe, which is that the precision improves for models with a fairly even spread of $\delta_{\mathbf{p}}$, while clustering of $\delta_{\mathbf{p}}$, a feature typical for models with large $|\mathcal{Z}^{K3\pi}|$, leads to reduced sensitivity.

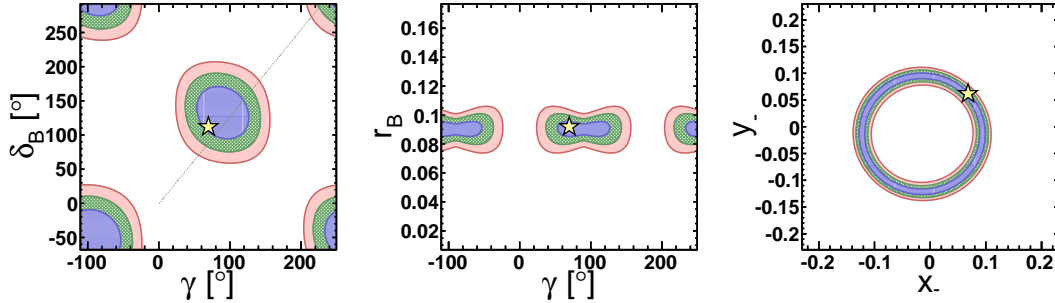


Figure 7. Constraints on r_B , δ_B , γ , x_- , y_- obtained using the phase-space integrated approach proposed in [7], with additional constraints from mixing [15]. In contrast to all other results shown in this letter, neither D mixing nor $B^\mp \rightarrow DK^\mp$ data are separated into multiple phase space bins. The study uses global constraints on $\mathcal{Z}^{K3\pi}$ extrapolated to BES III statistics [14], and the LHCb run II data scenario.

4.6 Additional input from the charm threshold

We consider two ways of incorporating additional information from the charm threshold. One is to incorporate constraints on the global coherence factor \mathcal{Z}^f . Such constraints are already available for $D \rightarrow K^-\pi^+\pi^-\pi^+$ and a few other decay modes, based on CLEO-c data [9, 13, 14], and could significantly improve with input from BES III, who have collected 3.5 times as much integrated luminosity at the charm threshold. These constraints can be added either to a phase-space integrated analysis of D mixing and $B^\mp \rightarrow DK^\mp$ as proposed in [15] or to the binned analysis introduced here. Alternatively, charm threshold data can be analysed in the same phase space bins as $B^\mp \rightarrow DK^\mp$ and charm mixing. This, as we will show below, will add additional information that substantially improves the measurement. Below we discuss each method in turn.

4.6.1 Phase-space integrated analysis with input from the charm threshold

In contrast to all other results presented in this letter, for this analysis, neither the charm mixing data, nor the $B^\mp \rightarrow DK^\mp$ data are divided into multiple phase space bins. We incorporate constraints on $\mathcal{Z}^{K3\pi}$ obtained from charm threshold data following [7], and perform fits to simulated data with and without input from a phase-space integrated D mixing analysis as proposed in [15]. Figure 7 shows confidence regions obtained for such a phase-space integrated analysis based on the LHCb run II scenario, with input from the charm threshold extrapolated to BES III statistics [14], including input from charm mixing. While with this method, there is insufficient information

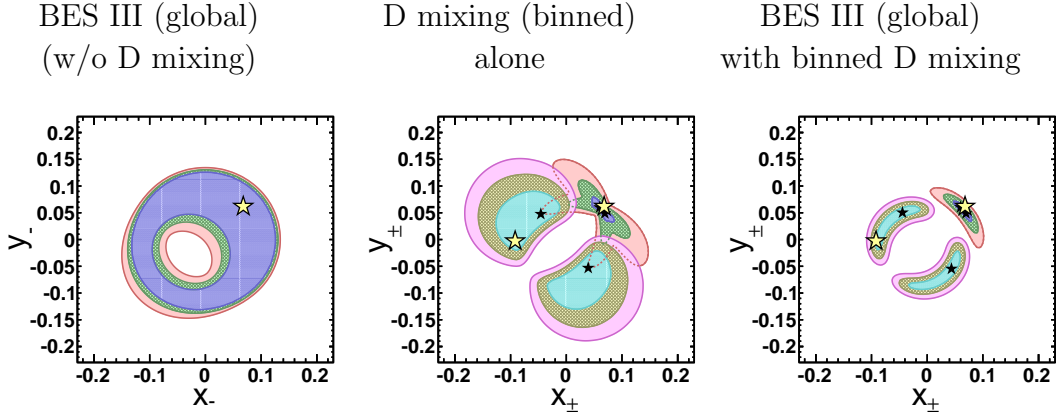


Figure 8. Constraints on x_{\pm} and y_{\pm} , obtained by combining simulated $B^{\mp} \rightarrow DK^{\mp}$ data (LHCb Run II statistics) with different constraints from charm. Left: future (BES III) charm threshold constraints on $\mathcal{Z}^{K3\pi}$ (only the effect on x_{-}, y_{-} is shown, results for x_{+}, y_{+} are similar). Centre: D mixing constraints. Right: Both. (Same format as in Fig. 4.)

to obtain point-estimates, 68% confidence regions can still be interpreted in terms of uncertainties on γ , δ_B and r_B , as described in Sec. 4.7. Averaging over 50 simulated experiments, we find $\sigma(\gamma) = 56^{\circ}$ (64°), $\sigma(\delta_B) = 53^{\circ}$ (66°) and $\sigma(r_B) = 0.92 \cdot 10^{-2}$ ($4.1 \cdot 10^{-2}$) with (without) input from D mixing. While the constraints on γ and δ_B are rather weak, the precision on r_B is excellent. As [14] have shown, input from such an analysis would play an important role in a global fit to measure γ .

4.6.2 Global constraints from the charm threshold, with a binned $B^{\mp} \rightarrow DK^{\mp}$ and D mixing analysis

Performing the fit on the absolute decay rates (see Sections 2.5 and 4.2) rather than the fractions, it is possible to incorporate constraints on the total coherence factor \mathcal{Z}^f from the charm threshold while still performing the binned analysis of $B^{\mp} \rightarrow DK^{\mp}$ and charm mixing data as described above, using the relation

$$\sum_{\text{all } \Omega_i} \mathcal{A}_{\Omega_i} \mathcal{B}_{\Omega_i} \mathcal{Z}_{\Omega_i}^f = \mathcal{A} \mathcal{B} \mathcal{Z}^f. \quad (4.4)$$

In the above expressions, $\mathcal{A}, \mathcal{B}, \mathcal{Z}^f$ are the equivalent quantities to $\mathcal{A}_{\Omega}, \mathcal{B}_{\Omega}, \mathcal{Z}_{\Omega}^f$ for a volume that encompasses the entire phase space. Figure 8 illustrates the significant benefit of such additional constraints, numerical results can be found in Tab. 2. The predicted BES III uncertainties on $\mathcal{Z}^{K3\pi}$ are taken from [14].

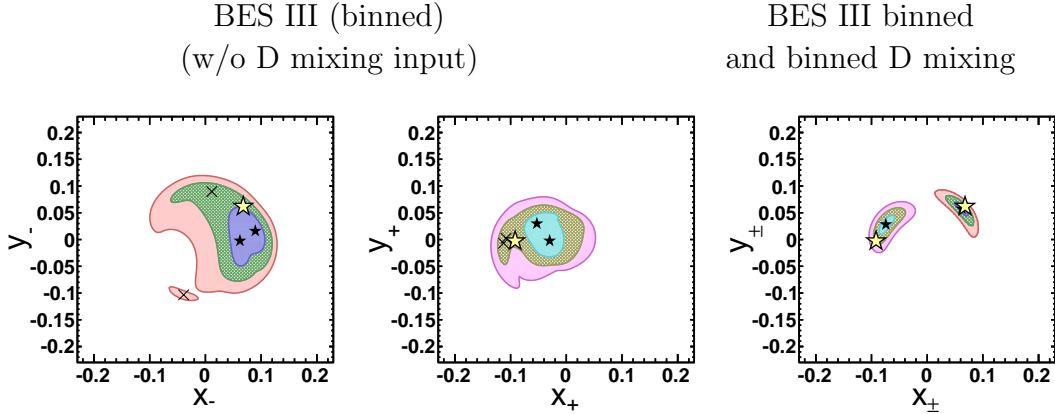


Figure 9. Constraints on x_{\pm} and y_{\pm} , obtained by combining simulated $B^{\mp} \rightarrow DK^{\mp}$ data (LHCb Run II statistics) with different constraints from charm. Two plots on the left: future (BES III) charm threshold constraints on binned $Z_{\Omega}^{K3\pi}$. Right: that, combined with D mixing. (Same format as in Fig. 4.)

4.6.3 Binned constraints from the charm threshold

In this section we compare the performance of a binned analysis relying on charm threshold data for the charm interference parameter, as proposed in [7], with the novel method proposed in this letter, and with a combined approach using binned threshold and charm mixing data. We analyse the charm threshold data in the same phase-space bins as $B^{\mp} \rightarrow DK^{\mp}$ and charm mixing. This provides a constraint from threshold data on each individual $Z_{\Omega}^{K3\pi}$, rather than only their weighted sum as in Sec. 4.6.2. To estimate the uncertainties on $Z_{\Omega}^{K3\pi}$ from such an analysis, we take the results on $\mathcal{Z}^{K3\pi}$ from [14], and assume that uncertainties scale with the inverse square-root of the number of signal events used for the measurement. Given the fairly large uncertainty on $\mathcal{Z}^{K3\pi}$ from CLEO-c data, we assume that these data can be divided into at most three bins while still providing meaningful constraints on $Z_{\Omega}^{K3\pi}$ in each bin. With BES III statistics, we expect it will be possible to match the binnings defined in Sec. 4.2, with up to eight bins. Figure 9 illustrates in the $x_{\pm} - y_{\pm}$ plane the dramatic effect that the combination of mixing constraints and binned $Z_{\Omega}^{K3\pi}$ constraints from a future analysis of BES III threshold data could have. Not only are the uncertainties on x_{\pm}, y_{\pm} much reduced compared to either constraint being applied individually (see Tab. 2 for numerical results), but the BES III input also removes the previously existing ambiguities in x_{\pm} and y_{\pm} . Figure 10, described below, confirms this observation for 1-dimensional parameters scans of x_{\pm} and γ .

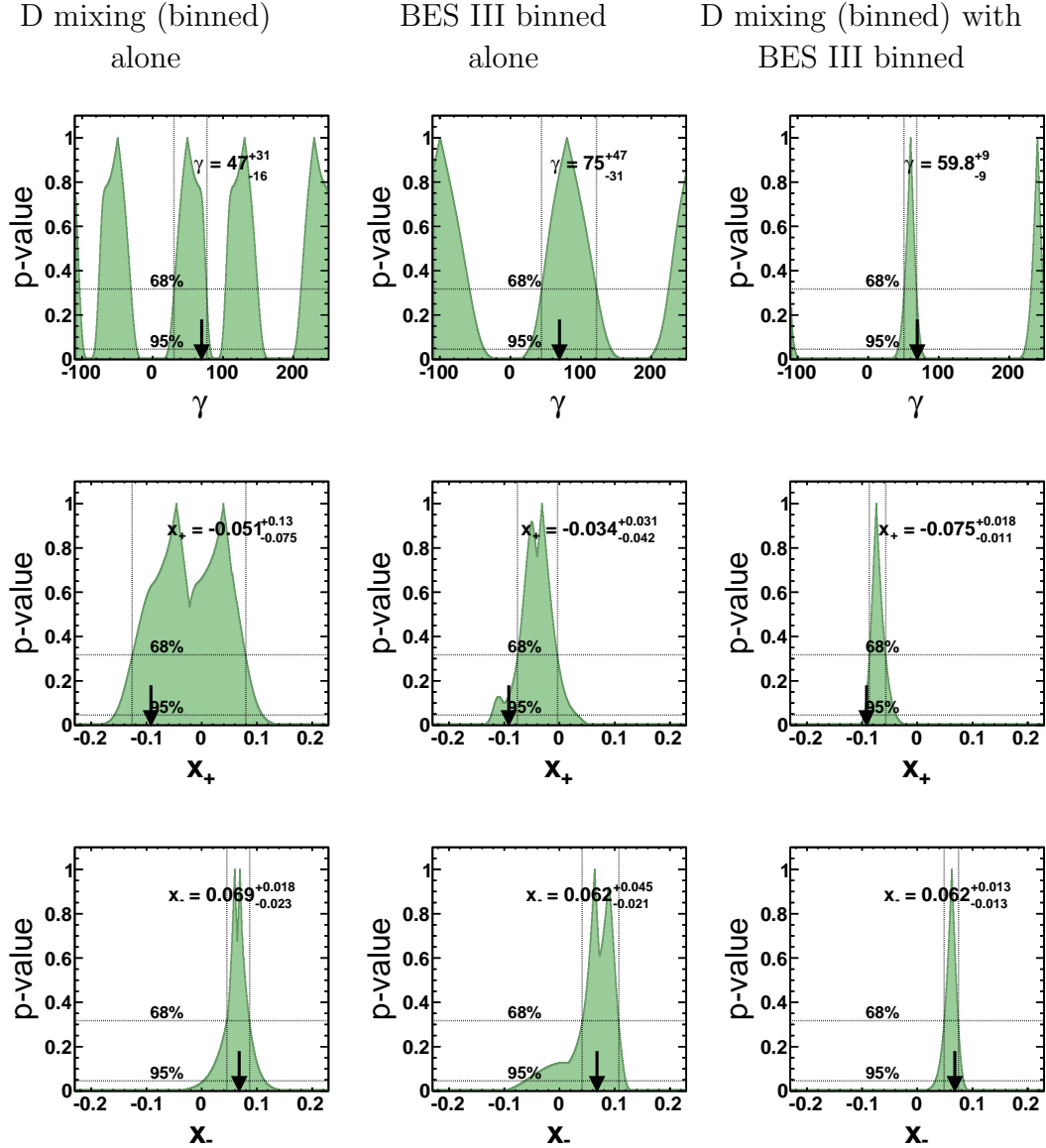


Figure 10. The p -value (see Eq. 4.3) versus γ , x_+ , and x_- for different charm inputs for estimated LHCb run II statistics. The arrow indicates the input value with which the experiment was simulated. The numbers inside the scans represent the best fit value $\pm 1\sigma$, as described in the text.

4.7 1-D scans and quantified uncertainties

We perform one-dimensional p -value (see Eq. 4.3) scans of the parameters of interest. To translate a scan into a numerical result for the uncertainty σ on a given parameter, we choose the peak associated to the fit result nearest the input value with which the

data were generated, and take half its width at $1 - p = 68\%$. We ignore multiple solutions, unless two solutions merge at the 68% CL level, in which case we take the width of the merged double-peak to calculate σ . This is illustrated for a few examples in Fig. 10.

4.8 Summary of results

Table 2 summarises our estimates of the uncertainties on the parameters describing CP violation in $B^\mp \rightarrow DK^\mp$, measured in $B^\mp \rightarrow DK^\mp$, $D \rightarrow K\pi\pi\pi$ for different charm inputs and data taking scenarios. These estimates are obtained from p -value scans as described above, averaged over 50 simulated experiments, generated using the default amplitude model.

The results indicate that an interesting precision on these parameters (especially x_- and y_-) can be achieved solely based on a combined analysis of $B^\mp \rightarrow DK^\mp$, $D \rightarrow K\pi\pi\pi$ and charm mixing data in several bins of the D decay’s phase space. Such a result would not provide a competitive measurement of γ by itself, but would be expected to make a valuable contribution to a combined fit, such as the ones described in [9, 14, 27].

However, using both charm input from mixing and from threshold data transforms this into a precision measurement of γ . While precise predictions are impossible until we have a better understanding of the $D^0 \rightarrow K^+\pi^-\pi^+\pi^-$ amplitude structure, the above results suggests that, with the approach proposed here applied to LHCb run 1 data, this channel can reach a similar precision as the combined analysis of $B^\mp \rightarrow DK^\mp$ with $D \rightarrow K_S\pi^+\pi^-$ and $D \rightarrow K_S K^+ K^-$ on LHCb run 1 data [39], currently the most precise individual measurement of γ in tree-level decays. Conversely, the inclusion of information from charm mixing leads to a vastly improved precision compared to that achievable based on charm input from threshold data alone, by about an order of magnitude for the upgrade scenario, emphasising the crucial role of the information from charm mixing.

Finally, our results indicate that the input from BES III has the potential to substantially improve the precision on γ over that achievable with CLEO-c’s dataset alone, especially if a binned analysis were to be performed. Further improvements would be expected from combining CLEO-c and BES III input, which, in this study, we only considered separately.

LHCb scenario	D^0 mix?	charm threshold?	$\sigma(\gamma)$ [°]	$\sigma(\delta_B)$ [°]	$\sigma(r_B)$ $\times 10^2$	$\sigma(x_+)$ $\times 10^2$	$\sigma(y_+)$ $\times 10^2$	$\sigma(x_-)$ $\times 10^2$	$\sigma(y_-)$ $\times 10^2$
run I			26	47	1.6	8.7	9.1	8.8	8.2
run II	Y	none	22	29	1.4	7.6	6.9	4.5	4.0
upgr			15	14	0.17	4.7	5.2	0.56	0.98
run I		CLEO global	20	29	0.82	6.4	5.7	6.6	5.9
run II	Y		15	19	0.62	5.4	3.9	2.5	2.7
upgr			11	10	0.16	3.8	2.8	0.44	0.50
run I		BESIII global	19	25	0.78	6.4	5.5	6.5	5.8
run II	Y		14	18	0.57	5.4	3.9	2.4	2.7
upgr			9.0	8.2	0.15	3.7	2.7	0.43	0.48
run I		CLEO binned	46	35	3.2	6.9	6.5	8.6	10
run II	N		50	34	3.3	6.9	6.7	8.9	11
upgr			52	35	3.3	7.6	6.7	8.9	11
run I		BESIII binned	40	24	2.6	4.1	5.0	5.7	6.2
run II	N		34	17	2.5	3.6	4.1	5.0	5.1
upgr			39	14	2.9	3.9	4.1	4.3	5.6
run I		CLEO binned	16	18	0.78	2.1	3.5	2.6	3.1
run II	Y		12	13	0.53	1.7	3.1	1.7	2.0
upgr			7.8	7.2	0.15	1.1	2.6	0.40	0.46
run I		BESIII binned	12	14	0.68	1.6	2.6	2.0	2.5
run II	Y		8.6	9.6	0.47	0.90	2.1	1.5	1.5
upgr			4.1	3.9	0.14	0.53	1.3	0.35	0.38

Table 2. Uncertainties on key parameters, obtained based on the default amplitude model in different configurations, averaged over 50 simulated experiments. All results are for the binned approach applied to $B^\mp \rightarrow DK^\mp$ and, where used, charm mixing data. The first column refers to the scenarios defined in Tab. 1. The second column defines whether charm mixing input was used (Y), or not (N). The third column describes additional input from the charm threshold. “CLEO global” refers to the phase-space integrated input from [14]. “BES III global” is the same, but uses the uncertainties predicted in [14] for a data sample 3.5 times as large as that collected by CLEO-c. “CLEO binned” and “BES III binned” extrapolate to a potential binned analysis of the charm threshold data described in Sec. 4.6.3.

5 Conclusion

We have presented a new method for the amplitude model-independent measurement of the CP violation parameter γ from $B^\mp \rightarrow DK^\mp$ decays, based on a combined analysis of

$B^\mp \rightarrow DK^\mp$ and charm mixing. When analysed in several bins of the D decay’s phase space, γ can be measured without additional input from the charm threshold. We have evaluated the performance of the method in a simulation study for the case where the D decays to $K^\pm\pi^\mp\pi^\pm\pi^\mp$, using sample sizes representing existing and plausible future datasets. The precision ultimately achievable depends on the $D^0 \rightarrow K^+\pi^-\pi^+\pi^-$ amplitude structure realised in nature, that we do not know. Our results suggest that the new method we introduced would, even without input from the charm threshold, provide valuable input to a global γ combination, although the precision would be insufficient to provide a competitive γ measurement in its own right.

We compare the performance of our novel method to that of a binned analysis with charm input from the threshold, as proposed in [7]. For the run I scenario, with BES III statistics, both methods perform similarly well. Assuming no additional data from the threshold, the mixing-based method introduced here performs significantly better for the LHCb-upgrade scenario, benefiting from the vast number of D events expected.

For all data taking scenarios we studied, combining the two methods results in a far superior performance than either can achieve individually. This is already the case when threshold data enter in the form of a phase-space integrated constraint on \mathcal{Z}^f , but by far the best results are obtained if D mixing, $B^\mp \rightarrow DK^\mp$ and charm threshold data are analysed in the same phase space bins. Such a combined approach transforms this into a highly competitive precision measurement of γ , on par with the best existing constraints from individual channels. Its precision keeps improving with charm mixing and $B^\mp \rightarrow DK^\mp$ event yields projected into the foreseeable future, even if no new data from the charm threshold become available.

Once a $D^0 \rightarrow K^+\pi^-\pi^+\pi^-$ amplitude model is available to inform the binning, the techniques we introduced here can be used to significantly improve the precision on γ and related parameters that can be obtained from $B^\mp \rightarrow DK^\mp$, $D \rightarrow K^\pm\pi^\mp\pi^\pm\pi^\mp$. Such a measurement would benefit greatly from an update of the $\mathcal{Z}^{K3\pi} = R_D^{K3\pi} e^{-\delta_D^{K3\pi}}$ measurement [9, 14] with BES III’s larger dataset, and, even more so, a binned $Z_\Omega^{K3\pi}$ analysis. With all of the above ingredients in place, the methods introduced in this letter, applied to $B^\mp \rightarrow DK^\mp$, $D \rightarrow K^\pm\pi^\mp\pi^\pm\pi^\mp$, could lead to one of the most precise individual γ measurements.

Its potential for other decay channels is yet to be evaluated.

Acknowledgments

We thank our colleagues from CLEO-c and LHCb for their helpful input to this paper, in particular Tim Gershon, Patrick Koppenburg, and Jim Libby. We acknowledge the

support from CERN, the Science and Technology Facilities Council (United Kingdom) and the European Research Council under FP7.

References

- [1] M. Gronau and D. Wyler, *On determining a weak phase from CP asymmetries in charged B decays*, *Phys.Lett.* **B265** (1991) 172–176.
- [2] M. Gronau and D. London, *How to determine all the angles of the unitarity triangle from $B_d \rightarrow DK_s$ and $B_s^0 \rightarrow D\phi$* , *Phys.Lett.* **B253** (1991) 483–488.
- [3] D. Atwood, I. Dunietz, and A. Soni, *Enhanced CP violation with $B \rightarrow KD^0(\bar{D}^0)$ modes and extraction of the Cabibbo-Kobayashi-Maskawa Angle γ* , *Phys.Rev.Lett.* **78** (1997) 3257–3260, [[hep-ph/9612433](#)].
- [4] A. Giri, Y. Grossman, A. Soffer, and J. Zupan, *Determining γ using $B^\pm \rightarrow DK^\pm$ with multibody D decays*, *Phys. Rev. D* **68** (Sep, 2003) 054018.
- [5] Belle Collaboration, A. Poluektov et al., *Measurement of ϕ_3 with dalitz plot analysis of $B^\pm \rightarrow D^{(*)}K^\pm$ decays*, *Phys. Rev. D* **70** (Oct, 2004) 072003.
- [6] J. Rademacker and G. Wilkinson, *Determining the unitarity triangle gamma with a four-body amplitude analysis of $B^+ \rightarrow (K^+K^-\pi^+\pi^-)_DK^\pm$ decays*, *Phys.Lett.* **B647** (2007) 400–404, [[hep-ph/0611272](#)].
- [7] D. Atwood and A. Soni, *Role of charm factory in extracting CKM phase information via $B \rightarrow DK$* , *Phys.Rev.* **D68** (2003) 033003, [[hep-ph/0304085](#)].
- [8] A. Giri, Y. Grossman, A. Soffer, and J. Zupan, *Determining gamma using $B^\pm \rightarrow DK^\pm$ with multibody D decays*, *Phys.Rev.* **D68** (2003) 054018, [[hep-ph/0303187](#)].
- [9] CLEO Collaboration, N. Lowrey et al., *Determination of the $D^0 \rightarrow K^-\pi^+\pi^0$ and $D^0 \rightarrow K^-\pi^+\pi^+\pi^-$ Coherence Factors and Average Strong-Phase Differences Using Quantum-Correlated Measurements*, *Phys.Rev.* **D80** (2009) 031105, [[arXiv:0903.4853](#)].
- [10] CLEO Collaboration, J. Libby et al., *Model-independent determination of the strong-phase difference between D^0 and $\bar{D}^0 \rightarrow K_{S,L}^0 h^+ h^-$ ($h = \pi, K$) and its impact on the measurement of the CKM angle γ/ϕ_3* , *Phys.Rev.* **D82** (2010) 112006, [[arXiv:1010.2817](#)].
- [11] CLEO Collaboration, R. A. Briere et al., *First model-independent determination of the relative strong phase between D^0 and $\bar{D}^0 \rightarrow K_s^0 \pi^+ \pi^-$ and its impact on the CKM Angle γ/ϕ_3 measurement*, *Phys.Rev.* **D80** (2009) 032002, [[arXiv:0903.1681](#)].

- [12] **CLEO** Collaboration, D. M. Asner et al., *Determination of the $D^0 \rightarrow K^+\pi^-$ Relative Strong Phase Using Quantum-Correlated Measurements in $e^+e^- \rightarrow D^0\bar{D}^0$ at CLEO*, *Phys.Rev.* **D78** (2008) 012001, [[arXiv:0802.2268](#)].
- [13] **CLEO** Collaboration, J. Insler et al., *Studies of the decays $D^0 \rightarrow K_S^0 K^- \pi^+$ and $D^0 \rightarrow K_S^0 K^+ \pi^-$* , *Phys.Rev.* **D85** (2012) 092016, [[arXiv:1203.3804](#)].
- [14] J. Libby et al., *New determination of the $D^0 \rightarrow K^- \pi^+ \pi^0$ and $D^0 \rightarrow K^- \pi^+ \pi^+ \pi^-$ coherence factors and average strong-phase differences*, *Phys.Lett.* **B731** (2014) 197–203, [[arXiv:1401.1904](#)].
- [15] S. Harnew and J. Rademacker, *Charm mixing as input for model-independent determinations of the CKM phase γ* , *Phys.Lett.* **B728** (2014) 296–302, [[arXiv:1309.0134](#)].
- [16] A. Bondar, A. Poluektov, and V. Vorobiev, *Charm mixing in the model-independent analysis of correlated $D^0 \bar{D}^0$ decays*, *Phys.Rev.* **D82** (2010) 034033, [[arXiv:1004.2350](#)].
- [17] **Belle** Collaboration, I. Adachi et al., *First measurement of ϕ_3 with a binned model-independent Dalitz plot analysis of $B^{+-} \rightarrow DK^{+-}$, $D \rightarrow K_s^0 \pi^+ \pi^-$ decay*, [[arXiv:1106.4046](#)].
- [18] **LHCb** Collaboration, R. Aaij et al., *A model-independent Dalitz plot analysis of $B^\pm \rightarrow DK^\pm$ with $D \rightarrow K_S^0 h^+ h^-$ ($h = \pi, K$) decays and constraints on the CKM angle γ* , *Phys. Lett.* **B718** (2012) 43–55, [[arXiv:1209.5869](#)].
- [19] **Heavy Flavor Averaging Group** Collaboration, Y. Amhis et al., *Averages of B -Hadron, C -Hadron, and tau-lepton properties as of early 2012*, [[arXiv:1207.1158](#)].
- [20] **LHCb** Collaboration, R. Aaij et al., *Measurement of $D^0 - \bar{D}^0$ mixing parameters and search for CP violation using $D^0 \rightarrow K^+ \pi^-$ decays*, *Phys.Rev.Lett.* **111** (2013) 251801, [[arXiv:1309.6534](#)].
- [21] **CDF** Collaboration, T. Aaltonen et al., *Evidence for $D^0 - \bar{D}^0$ mixing using the CDF II Detector*, *Phys.Rev.Lett.* **100** (2008) 121802, [[arXiv:0712.1567](#)].
- [22] **Belle** Collaboration, M. Staric et al., *Evidence for $D^0 - \bar{D}^0$ Mixing*, *Phys.Rev.Lett.* **98** (2007) 211803, [[hep-ex/0703036](#)].
- [23] **BaBar** Collaboration, B. Aubert et al., *Evidence for $D^0 - \bar{D}^0$ Mixing*, *Phys.Rev.Lett.* **98** (2007) 211802, [[hep-ex/0703020](#)].
- [24] **BaBar** Collaboration, B. Aubert et al., *Measurement of $D^0 - \bar{D}^0$ mixing from a time-dependent amplitude analysis of $D^0 \rightarrow K^+ \pi^- \pi^0$ decays*, *Phys.Rev.Lett.* **103** (2009) 211801, [[arXiv:0807.4544](#)].
- [25] **BaBar** Collaboration, B. Aubert et al., *Measurement of $D^0 - \bar{D}^0$ Mixing using the*

- Ratio of Lifetimes for the Decays $D^0 \rightarrow K^- \pi^+$ and $K^+ K^-$* , *Phys.Rev.* **D80** (2009) 071103, [[arXiv:0908.0761](#)].
- [26] **LHCb** Collaboration, R. Aaij et al., *Observation of $D^0-\bar{D}^0$ oscillations*, *Phys. Rev. Lett.* **110** (2013) 101802, [[arXiv:1211.1230](#)].
- [27] **LHCb** Collaboration, R. Aaij et al., *Measurement of the CKM angle γ from a combination of $B^\pm \rightarrow Dh^\pm$ analyses*, *Phys.Lett.* **B726** (2013) 151–163, [[arXiv:1305.2050](#)].
- [28] **LHCb** Collaboration, *Improved constraints on γ from $B^\pm \rightarrow DK^\pm$ decays including first results on 2012 data*, *LHCb-CONF-2013-006* (2013).
- [29] M. Rama, *Effect of D - \bar{D} mixing in the extraction of gamma with $B^- \rightarrow D^0 K^-$ and $B^- \rightarrow D^0 \pi^-$ decays*, *Phys.Rev.* **D89** (2014) 014021, [[arXiv:1307.4384](#)].
- [30] **Mark III** Collaboration, D. Coffman et al., *Resonant substructure in $\bar{K}\pi\pi\pi$ decays of d mesons*, *Phys. Rev. D* **45** (Apr, 1992) 2196–2211.
- [31] **LHCb** Collaboration, R. Aaij et al., *Model-independent search for CP violation in $D^0 \rightarrow K^- K^+ \pi^- \pi^+$ and $D^0 \rightarrow \pi^- \pi^+ \pi^- \pi^+$ decays*, [[arXiv:1308.3189](#)].
- [32] A. Bondar and A. Poluektov, *On model-independent measurement of the angle $\phi(3)$ using Dalitz plot analysis*, [[hep-ph/0703267](#)].
- [33] **LHCb** Collaboration, R. Aaij et al., *Observation of the suppressed ADS modes $B^\pm \rightarrow [\pi^\pm K^\mp \pi^+ \pi^-]_D K^\pm$ and $B^\pm \rightarrow [\pi^\pm K^\mp \pi^+ \pi^-]_D \pi^\pm$* , *Phys. Lett.* **B723** (2013) 44, [[arXiv:1303.4646](#)].
- [34] **LHCb** Collaboration, I. Bediaga et al., *Framework TDR for the LHCb Upgrade: Technical Design Report*, Tech. Rep. CERN-LHCC-2012-007, CERN, Apr, 2012.
- [35] **Heavy Flavor Averaging Group** Collaboration, Y. Amhis et al., *Averages of B -Hadron, C -Hadron, and tau-lepton properties as of early 2012.*, [[arXiv:1207.1158](#)]. Regular online updates, we use CHARM 2013 averages.
- [36] **Particle Data Group** Collaboration, J. A. Olive et al., *Review of Particle Physics*, *Chin.Phys.* **C38** (Aug, 2014) 090001.
- [37] D. M. Kunze, D. S. Gabriel, and D. A. Garcia, *Distributed parametric optimization with the Geneva library*, in *Data Driven e-Science* (S. Lin and E. Yen, eds.), p. 303, Springer, 2011.
- [38] F. James, *MINUIT Function Minimization and Error Analysis: Reference Manual Version 94.1*, *CERN-D-506* (1994).
- [39] **LHCb** Collaboration, R. Aaij et al., *Measurement of the CKM angle γ using $B^\pm \rightarrow DK^\pm$ with $D \rightarrow K_S^0 \pi^+ \pi^-$, $K_S^0 K^+ K^-$ decays*, *JHEP* **1410** (2014) 97, [[arXiv:1408.2748](#)].